

# Abdominal-Deformation Measurement for a Shape-Flexible Mannequin Using the 3D Digital Image Correlation

**Huan Liu**

Engineering Research Center of Digital Textile & Apparel Technology, Ministry of Education, College of Information Science and Technology, Donghua University, Shanghai, China

Key Laboratory of Watershed Ecology and Geographical Environment Monitoring NASG, Jinggangshan University & College of Electronic and Information Engineering, Jinggangshan University, Ji'an, Jiangxi, China

liuhuan816618@163.com

**Kuangrong Hao\* and Yongsheng Ding**

Engineering Research Center of Digital Textile & Apparel Technology, Ministry of Education, College of Information Science and Technology, Donghua University, Shanghai, China

krhao@dhu.edu.cn

## Abstract

In this paper, the abdominal-deformation measurement scheme is conducted on a shape-flexible mannequin using the DIC technique in a stereo-vision system. Firstly, during the integer-pixel displacement search, a novel fractal dimension based on an adaptive-ellipse subset area is developed to track an integer pixel between the reference and deformed images. Secondly, at the subpixel registration, a new mutual-learning adaptive particle swarm optimization (MLADPSO) algorithm is employed to locate the subpixel precisely. Dynamic adjustments of the particle flight velocities that are according to the deformation extent of each interest point are utilized for enhancing the accuracy of the subpixel registration. A test is performed on the abdominal-deformation measurement of the shape-flexible mannequin. The experiment results indicate that under the guarantee of its measurement accuracy without the cause of any loss, the time-consumption of the proposed scheme is significantly more efficient than that of the conventional method, particularly in the case of a large number of interest points.

**Category:** Computer Graphics / Image Processing

**Keywords:** Abdominal-deformation measurement; 3D digital-image correlation; Integer-pixel displacement search; Subpixel-registration resolution; Mutual-learning adaptive particle swarm optimization (MLADPSO)

## I. INTRODUCTION

The morphology of the human body, especially the belly shape, is a crucial factor in areas such as apparel-customized services and body fitness. It is widely accepted that the accurate and effective attainment of the belly size and a building of a 3D belly profile are critical for the

provision of a vital reference value for human fashion design. Generally, the existing studies concerning the measurement of the human-belly shape have been undertaken using a static scheme [1, 2]; however, the deformation measurement for different shapes should be taken into account in personalized fashion design. Unfortunately, a dearth exists regarding the studies that

**Open Access** <http://dx.doi.org/10.5626/JCSE.2017.11.3.79>

<http://jcse.kiise.org>

This is an Open Access article distributed under the terms of the Creative Commons Attribution Non-Commercial License (<http://creativecommons.org/licenses/by-nc/3.0/>) which permits unrestricted non-commercial use, distribution, and reproduction in any medium, provided the original work is properly cited.

Received 18 January 2017; Revised 19 July 2017; Accepted 08 September 2017

\*Corresponding Author

consider this topic, so it is believed that the dynamic deformation measurement will become a salient future issue.

Digital image correlation (DIC) [3, 4] is a powerful and well-established noncontact optical metrology that is based on computer vision for full-field surface-deformation measurements. The DIC method that can be classified into 2D and 3D categories was first proposed by Peters and Ranson [5] in the 1980s. The 2D DIC with a single camera has been applied to a large variety of research fields [6], while the advanced 3D DIC [7] is utilized for 3D profile and deformation measurements due to its extreme practicality and effectiveness. Pan et al. [8] employed the pixel voxel to retrieve 3D deformed information. Pan and Wang [9] performed a DIC comparison of two subpixel-registration algorithms. The DIC method has been applied to the measurement of the dynamic foot-surface shape during the walking process [10]. Until the present time, the DIC technique has been improved significantly with the incorporation of gray interpolation methods [11], the shape function [12], the subset size [13], and various subpixel-registration algorithms [14].

DIC, however, is still limited by significant drawbacks that result in dissatisfactory effects in the practical applications. This problem is attributed to the following three issues. Firstly, it is assumed that an object deforms continuously and the gray-level intensity is constant, but when it confronts a large deformation, it is difficult to conform the supposition to the actual situation. The subsequent linear and nonlinear formulas are presented in the literature [15]. Nevertheless, this issue dramatically increases the cost that is owing to the additional parameters. Secondly, the common ideology deems that a set of adjacent points in a reference subset remains as the neighboring points in the target subset and the size of the rectangle subset is fixed. To address the DIC problems, the literature [16] discussed a number of improvement techniques including the first-order shape function and the second-order shape function. Undoubtedly, all of these improvements raise the complexity and the computational cost extremely. Finally, the feature points do not remain at the integer-pixel positions after a deformation. It is difficult to achieve the acceptable accuracy with a mere reliance on the integer-pixel search; consequently, the subpixel registration is indispensable. Substantial studies and experiments have proven that the Newton-Raphson (NR), Levenberg-Marquard (LM), and quasi-Newton (qN) methods are accurate and effective subpixel-registration algorithms. But the disadvantages of these algorithms that have been revealed in recent years, such as huge computational costs and local minimums with untrue values that make it difficult to satisfy the time-critical demands in real-time applications, need to be considered.

To avoid the previously mentioned drawbacks, the literature [17] developed an improved genetic algorithm (GA) for the subpixel registration of dual-energy computed

tomography (CT) images. Most recently, particle swarm optimization (PSO) was successfully implemented to optimize the correlation coefficient function derived by literature [18]. A novel optimization algorithm that is based on the improved GA and the PSO was used to optimize the parameters in a least squares support vector machine (LS-SVM) [19]. More important, the design of the algorithm still comprises strict requirements regarding the initial deformation guess. Zhang et al. [20] presented a hand-operated and computer-controlled interactive method. In this method, three or more distinct points on the undeformed image and their corresponding locations on the deformed image are identified manually. This approach is simple but not intelligent because of the low extent of automatization.

Lately, the fractal dimension of fractal geometry has been gradually developed as a quite active mathematic branch. The fractal analysis has been extensively used for the image analysis [21], feature extraction and matching [22, 23], pattern recognition [24], computer vision [25], and composite-material 3D reconstruction [26]. Its main characteristics are self-similarity and the calibration invariance.

In view of the previously mentioned deficiencies, the primary contributions of the paper can be summarized concisely as follows:

1. A novel feature vector consisting of a fractal dimension and a main subset direction is used for integer-pixel mapping based on the fractal-dimension theory.
2. Under the situation of an actual background, an elliptic subset is proposed according to an analysis of the deformation shape, while the subset size is simultaneously allowed to adjust adaptively in accordance with the deformation degree.
3. With a mutual-learning adaptive-PSO (MLADPSO) algorithm, integer-pixel positions that are obtained from a coarse search are regarded as the initial-guess estimations for the subpixel locations.

The goal of this paper is the exploitation of a novel methodology that enables an automatic measurement of the changed abdominal shape for different size groups.

The rest of this paper is organized as follows: The basic principle as well as the technology of the 3D DIC technique is presented in Section II; the details of the improved strategies are expounded in Section III; the results of numerical experiments and tests are discussed in Section IV; and lastly, the drawn conclusions are presented in Section V.

## II. FUNDAMENTAL PRINCIPLE AND TECHNOLOGY FOR THE 3D DIC

### A. Basic Principles of the Integer-Pixel Search

The existing DIC algorithm involves the following two

major steps: integral pixel (i.e., coarse search) and subpixel registration (i.e., fine search). In the integral-pixel search, the process comprises the tracking of the gray-value pattern in a small neighborhood called the *subset*. In general, a rectangle is centered at the interrogated point between the reference image and the deformed image. During the coarse search, the displacement field within the subset is assumed to be continuous and smooth. Besides, the movement of the displacement increment is constrained by an integer number of the spacing between the pixels. The tracking procedure is completed by a search for the peak position of the correlation-coefficient distribution. Once the maximum similarity is detected, the shape and the position of the target subset within the deformed image can be determined. The procedure is accomplished when all of the interest points have successfully obtained their own corresponding optimal points in the deformed image.

Nevertheless, it is necessary to mention that the feature points may become located between the pixels (i.e., subpixel location) while the deformation occurs. Thus, it is difficult to conform to the required precision in practical applications because of the derivation from the integer-pixel location. Undoubtedly, the fine-search resolution is considered as a critical technique for the improvement of the accuracy of the DIC method in the cases of certain hardware conditions.

## B. Formalism of the Subpixel-Registration Resolution

The principle of the subpixel-registration resolution is shown in Fig. 1, where  $p$  is a center point in the reference subset at the coordinate  $(x_0, y_0)$ , and the size is set as  $(2M+1) \times (2M+1)$ , called the *sample subset*; this sample subset corresponds to a subset in the deformed image called the *target subset* with another center point  $p'$  at the coordinate  $(x'_0, y'_0)$ , where  $q$  is a random point in the reference subset at the coordinate  $(x_i, y_j)$ . The corresponding point in the target subset at the coordinate  $(x'_i, y'_j)$  is  $q'$ , the displacement of which can be calculated using the following three mapping functions: *zero-order shape function*, *first-order shape function*, and *second-order shape function*.

The Newtonian algorithm, combined with a robust matching criterion and a high-accuracy subpixel registration, has been referred to as the gold standard for the subpixel registration. The Newtonian algorithm solves the nonlinear equations by directly employing the regularized cross-correlation coefficient as the optimization function. Pan and Li [27] put forward an improved NR method for the reduction of its complexity, enhancing its computational efficiency as well as strengthening its robustness. In spite of its achievement of the most accurate subpixel estimation, one significant shortcoming of the Newtonian algorithm is an extremely huge computational cost that is mainly

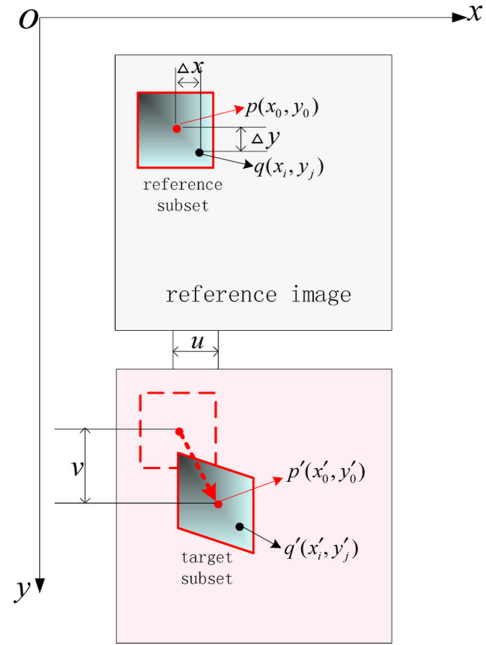


**Fig. 1.** Diagram of the digital image correlation (DIC) between the reference and deformed images.

due to its calculations of the first-order and second-order derivatives, especially regarding the  $6 \times 6$  Hessian matrix.

## C. 3D DIC based on Stereo Vision

Stereo vision [28] generally serves as a technique for the implementation of the 3D surface-profile reconstruction on the basis of two matched points from two different viewpoints. As shown in Fig. 2, the whole mapping process comprises the following two parts: stereo-matching in the horizontal part and the temporal matching between the original and deformed images from the same camera in the vertical part.  $p_l$  is a point in the left reference image at  $t_i$ , and its matching point in the right image is  $p_r$ . When the deformation occurs,  $p_l$  moves to a new position  $p'_l$  in the left reference image at  $t_{i+1}$ , and its matching point in the right deformed image also moves to  $p'_r$ . In this paper, the main focus is on the temporal-mapping procedure. Then, a series of improved alternative strategies are provided for the purpose of solving the substantial difficulties that often arise in deformation situations.

## III. PROPOSED IMPROVED STRATEGIES

### A. Novel Integer-Pixel Displacement-Search Method

#### 1) Innovation of the Fractal Dimension based on the Subset Area

The fractal dimension is an essential application in

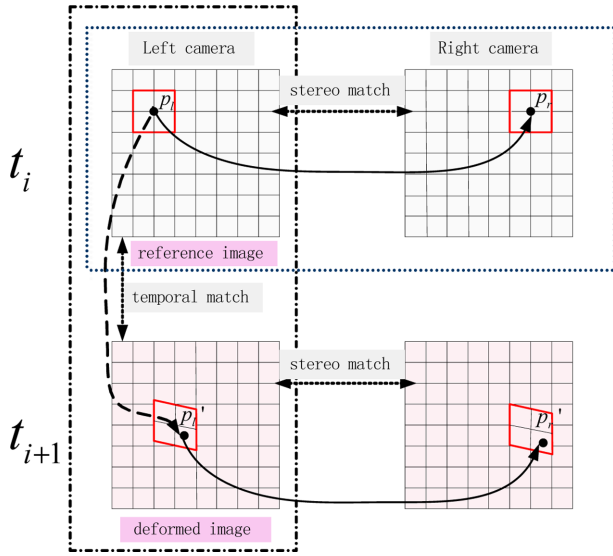


Fig. 2. Diagram of 3D DIC matching process.

image processing. There are numerous ways to calculate the fractal dimension. In general terms, the box dimension is widely applied in image processing, where the entire area of an image is filled with boxes of the size  $\delta$  (i.e., a cover). The variation of the size of  $\delta$  causes the changes of the number of the boxes  $N_\delta$ ; that is, the smaller the size of  $\delta$ , the higher the number of boxes.

The normal box-counting method of the fractal dimension for which the image is used is defined as follows:

$$D = \lim_{\delta > 0} \frac{\ln(N_\delta)}{\ln(1/r)}, \quad (1)$$

where  $N_r$  denotes the requisite total box quantity for the coverage of the whole image, and  $r$  is the side of the box (i.e., the cover of  $r$ ). A series of  $N_r$  can be obtained by a list of different  $r$  values, where  $\ln(1/r)$  is taken as the x-axis,  $\ln(N_r)$  is taken as the y-axis, and then the box dimension is a straight-line gradient that is obtained by means of the method of least squares.

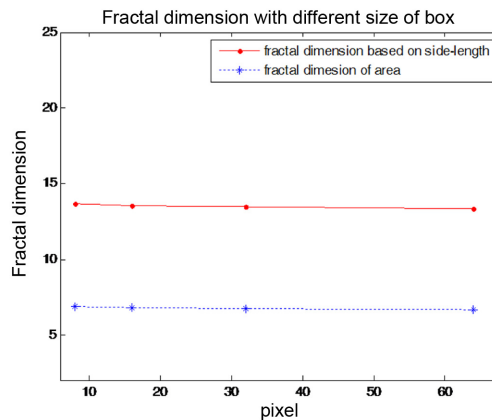
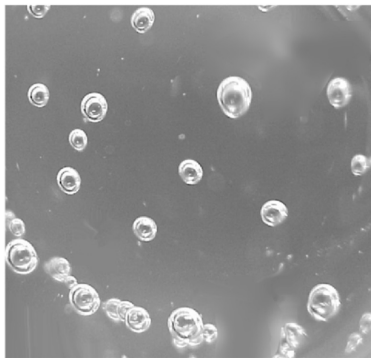


Fig. 3. Fractal dimensions of different forms.

The number of each cover is solely considered in Eq. (1), so the gray-level intensity and the probability for each cover are the substitutions of its numerator. Alternatively, by allowing for a variation of the side of the box according to the same proportion when the covered range is varied, the size ratio replaces the denominator in Eq. (1), and the new form is described as follows:

$$D_r = \lim_{\delta > 0} \frac{\sum f(i) \times p_i \times \ln(p_i)}{\ln(R/r)}, \quad (2)$$

where  $R$  represents the image size.

The denominator in Eq. (2) can be also modified using the area ratio that is expressed, as follows:

$$D_s = \lim_{\delta > 0} \frac{\sum f(i) \times p_i \times \ln(p_i)}{\ln(S/s_r)} = \lim_{\delta > 0} \frac{\sum f(i) \times p_i \times \ln(p_i)}{\ln(R^2/r^2)} = \frac{1}{2} D_r. \quad (3)$$

As can be seen, the fractal dimension of the area is half of the side value, and this ensures a shortening of the deviations between the different scales. This is demonstrated in Fig. 3, wherein the fractal-dimension calibration independence under the different-size conditions is implied.

### 2) Adaptive Adjustment of the Elliptic Subset

A rectangle subset is commonly employed in DIC. Actually, the shape of the correlated subset deforms in the large deformation that is shown in Fig. 4(a) and (b). Besides, with no deformation, the difference in the number of pixels that belong to the same-size subset is nonexistent. Whereas if the deformation of the object surface occurs, the quality of the pixels will change from the original to the deformed images, and this occurs even in subsets of the same size.

In this work, the tests of the abdominal-deformation measurement are conducted on a shape-flexible model with an installed gasbag. The representations of the existing studies show that the gasbag during its inflation can be regarded as a ball. Thus, the elliptic subset that is

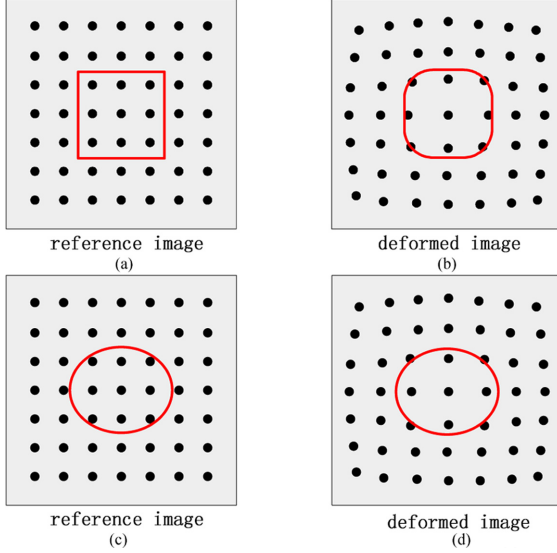


Fig. 4. Subset of the deformation.

displayed in Fig. 4(c) and (d) is proposed. The subset-size accuracy is considered as a critical factor that is close to the accuracy of the measured displacement. A too-small subset size tends to result in a deterioration of the accuracy, while a too-large subset may cause an excessive computational cost. So the suitable size is achieved with a balance of the influences of the random and systematic errors.

It is clearly preferable to search a parameter to define the image-deformation degree on the basis of a subset. By doing so, it is practicable to evaluate the effect of the image-structure information of each image subset on the deformation measurement. To serve this purpose, an intuitive parameter called *subset structure density* is proposed here, whereby the subset size can be judged dynamically using the structural density depending on the extent of the deformation, as shown in Fig. 4(d).

$$\Gamma = \frac{\sum |f_i - \bar{f}_i|^2}{A} \bigg/ \left( \frac{1}{A} (\sum |f_i - \bar{f}_i|) \right)^2, \quad (4)$$

where  $f_i$  signifies the gray-level intensity within the subset,  $\bar{f}_i$  denotes the mean of the gray-level intensity, and  $A$  is the gray number within the subset.

To ensure the reliability of the matching in the design of the adaptive subset, three steps are included. In the first place the major axis of the original elliptic size is set as 8 pixel and the minor axis is set as 6 pixel; in the second place, the associated  $\Gamma$  within the subset is determined and simultaneously set as the threshold; and finally, the new subset is acquired by an enlargement or reduction using the Step-2 pixels on the basis of the original size.

Moreover, without a direction factor, which may cause an error because of the insufficiency of the information

that is derived from the fractal dimension, the direction property that is required for the feature descriptor should be involved within the elliptic subset. The main direction is determined by the distribution of the peak gradient directions within the adjacent pixels around the key point. Therefore, the above proposed feature descriptor can be modified as a feature vector by

$$feature = [fractal \ dimension, \ main \ direction].$$

Next, the adoption of the distance between the two feature vectors as the criterion of the similarity measurement of each interest corner proceeds as follows:

$$S_{ij} = \exp[-|F_l(i) - F_r(i)|],$$

where  $|F_l(i) - F_r(i)|$  is termed as a distance measurement that is determined by

$$|F_l(i) - F_r(i)| = |fd_l(i) - fd_r(i)| \cdot |md_l(i) - md_r(i)|,$$

where  $fd$  denotes the fractal dimension and  $md$  is the main direction.

In specific applications, a suitable threshold for the similarity needs to be set in accordance with the accuracy requirement. If the similarity is greater than the threshold value, then the matching pair can be accepted and retained. The smaller the threshold value, the fewer the number of correct matchings, while a higher precision results in a more stable system.

## B. MLADPSO Algorithm for the Subpixel Registration

The PSO is a stochastic algorithm. Literature [29] presented an improved PSO method for the parameter optimization of the image-distortion correction and mosaicking in a panoramic parking-assistant system for the automotive aftermarket. In literature [30], an adaptive PSO is introduced to estimate the real transformation angle for the sample point. In this paper, a novel MLADPSO algorithm that is utilized for the subpixel registration is introduced. The MLADPSO is an improvement based on the standard PSO that involves both an information mutual-learning mechanism and a dynamic adaptive-adjustment ideology in terms of the PSO. The operation of an adaptive regulation of the particle velocities ensures adaptability and diversity, and this plays a role in the avoidance of the trapping within the local extremum and results in fewer iterations. Besides, the previous optimal information is fully used in the initialization of the particle positions regarding the next feature point, which effectively improves the speed of the convergence.

In the uniform PSO, the learning factors  $r_1$  and  $r_2$ , which are adopted to weigh the searching ability, were generally set at 2 empirically. For the sake of the closed

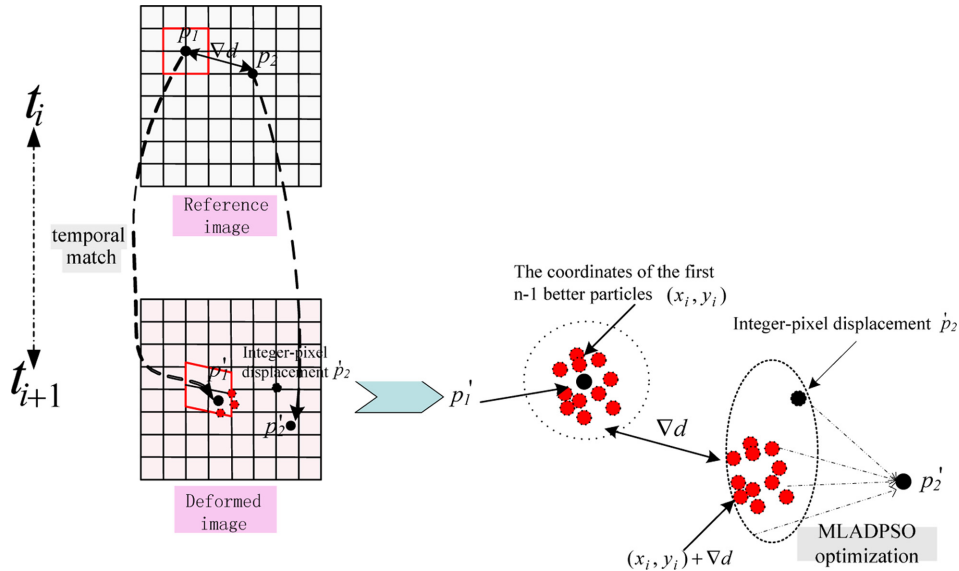


Fig. 5. The mutual-learning dynamic adaptive-particle swarm optimization (MLADPSO) diagram.

relation between the flight velocity and the range, it is indispensable to adaptively adjust the flight velocity. In this paper, an asynchronous strategy is implemented to adjust the learning factors to enhance the optimization. Considering the deformation differences of  $x$  and  $y$  in relation to the deformed-belly image,  $r_1$  and  $r_2$  were further refined into  $r_{1x}$  and  $r_{1y}$  and  $r_{2x}$  and  $r_{2y}$ , respectively.

It is assumed that the structural density of each feature point in the reference image is denoted by  $\Gamma_{reference} = \{\Gamma_{r1}, \Gamma_{r2}, \Gamma_{r3}, \dots, \Gamma_{rn}\}$ , while in the deformed image, it is denoted by  $\Gamma_{deformed} = \{\Gamma_{d1}, \Gamma_{d2}, \Gamma_{d3}, \dots, \Gamma_{dn}\}$ , and the variations between these two values can be expressed as  $\Delta\Gamma = \{\Delta\Gamma_1, \Delta\Gamma_2, \Delta\Gamma_3, \dots, \Delta\Gamma_n\}$ .  $r_1$  and  $r_2$  are assigned as follows:

$$r_1 = \begin{cases} r_{1m} & \Delta\Gamma_i = \max \Delta\Gamma \\ \frac{\Delta\Gamma_i}{\max \Delta\Gamma} \cdot r_{1m} & \Delta\Gamma_i = \min \Delta\Gamma, \quad (5) \\ \frac{\Delta\Gamma_i - \min \Delta\Gamma}{\max \Delta\Gamma - \min \Delta\Gamma} \cdot r_{1m} & \text{otherwise} \end{cases}$$

$$r_2 = \begin{cases} r_{2m} & \Delta\Gamma_i = \max \Delta\Gamma \\ \frac{\Delta\Gamma_i}{\max \Delta\Gamma} \cdot r_{2m} & \Delta\Gamma_i = \min \Delta\Gamma, \quad (6) \\ \frac{\Delta\Gamma_i - \min \Delta\Gamma}{\max \Delta\Gamma - \min \Delta\Gamma} \cdot r_{2m} & \text{otherwise} \end{cases}$$

where, generally,  $r_{1m} = r_{2m} = 2$  when the pixel deformation degree reaches the largest vales of  $r_1 = r_{1m} = 2$  and  $r_2 = r_{2m} = 2$ . The others are determined linearly according to the deformation degree.

The values  $r$  of the x-axis and the y-axis are respectively defined by

$$\begin{cases} r_{1x} = \frac{x_d - x_r}{x_d} r_1 \\ r_{2x} = \frac{x_d - x_r}{x_d} r_2 \end{cases} \quad (7)$$

$$\begin{cases} r_{1y} = \frac{y_d - y_r}{y_d} r_1 \\ r_{2y} = \frac{y_d - y_r}{y_d} r_2 \end{cases}, \quad (8)$$

where  $x_r$  and  $y_r$  are the coordinates in the reference image,  $x_d$  and  $y_d$  are the coordinates in the deformed image, and  $\frac{x_d - x_r}{x_d}$  and  $\frac{y_d - y_r}{y_d}$  indicate the deformed degradation on the x- and y-axes, respectively.

As shown in Fig. 5, with the aim of a search for the matched point with a higher precision in the right-view image that encounters the belly deformation for each detected corner in the reference image, the MLADPSO is implemented to obtain the subpixel coordinate values. In the MLADPSO, the parameters of each particle are referred to as the x- and y-coordinate values of each interest point. The number of particles is located at  $N$ . The initial values of the particle in the first iteration incorporate the integer-pixel value, namely  $p_r(x_{coarse}, y_{coarse})$ , derived from the integer-pixel displacement in the stereo matching, as well as the n-1 of the distance ( $\Delta d$ ) values based on  $p_r(x_{coarse}, y_{coarse})$ . In the temporal matching, the  $\Delta d$  that is set randomly signifies the relative distance for the points such as  $p_i$  and  $p_i'$  in the reference and deformed images from the left view. The parametric n-1 can be denoted as  $(p_r + \Delta d_1, p_r + \Delta d_2, \dots, p_r + \Delta d_{n-1})$ , and then the global best value  $(x_{gbest}, y_{gbest})$  can be gained after multiple iterations. Next, with regard to the rest of the



corners in the reference image, the initialization of the particles is defined in accordance with the mutual-learning property. The particle parameters are denoted as  $((x_{gbest(1)}^{i-1}, y_{gbest(1)}^{i-1}) + \Delta d_1, (x_{gbest(2)}^{i-1}, y_{gbest(2)}^{i-1}) + \Delta d_2, \dots, (x_{gbest(n-1)}^{i-1}, y_{gbest(n-1)}^{i-1}) + \Delta d_{n-1})$ , and in the integer-pixel displacement stage, its own integer-pixel coordinate value is  $p_i(x_{coarse}^i, y_{coarse}^i) \cdot ((x_{gbest(1)}^{i-1}, y_{gbest(1)}^{i-1}), (x_{gbest(2)}^{i-1}, y_{gbest(2)}^{i-1}), \dots, (x_{gbest(n-1)}^{i-1}, y_{gbest(n-1)}^{i-1}))$  are the top best n-1 values from the former corner, and in the temporal matching,  $\Delta d'$  signifies the relative distances of  $p_{l(i-1)}$  and  $p_{l(i)}$  in the deformed image from the left view. The entire process continues until the subpixel registrations of all of the feature points are fulfilled.

#### IV. EXPERIMENTS AND ANALYSIS

##### A. Experimental Setup

In this section, the conduction of the experiments on the belly-deformation measurements of the shape-flexible model using the proposed methods is reported. The specific setup that is shown in Fig. 6 consists of the following two main parts: (I) A shape-flexible model with an installed airbag, as can be seen in Fig. 6(a); an electric air pump that is shown in Fig. 6(b); and the software platform of Fig. 6(c). The electric air pump uses the inflation of the airbag to vary the shape on the abdomen with different pressures. (II) A stereo-vision system composed of four Cyber-shot DSC-W3 CMOS cameras (Sony, Japan) with a resolution of  $2816 \times 2112$  and an effective pixel quantity of approximately 6003000 pixel, as shown in Fig. 7, was utilized. The focal length of 18.9 mm (when it is converted to the 135-mm camera, the value is 114 mm) is arranged around the model, and the image size is  $624 \times 363$  pixel. Two of the cameras (NO. 1 and NO. 2) were located as a pair at the front of the abdomen at an angle of  $60^\circ$ , and

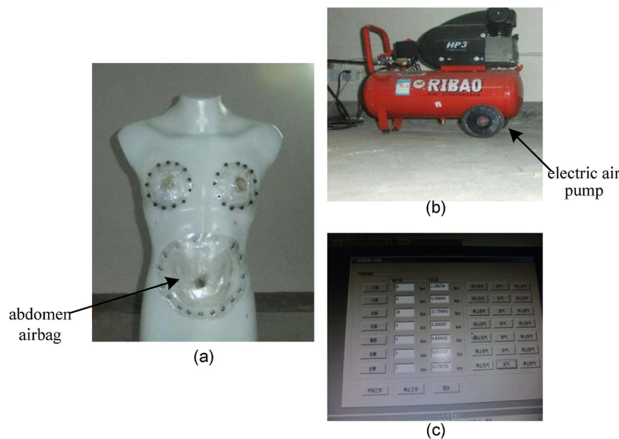


**Fig. 6.** Experimental setup. (a) A shape-flexible model with an installed airbag, (b) an electric air pump, and (c) the software platform.

the other two cameras (NO. 3 and NO. 4) were arranged at the rear of the abdomen at the same angle. The frontal cameras were used to obtain the abdominal images, and the rear ones captured the images from the back part of the abdomen.

The abdominal images from the different perspectives are shown in Fig. 8. For a straightforward extraction of the feature points, a portion of the seams of a tight dress that was fitted onto the abdominal part of the shape-flexible model served as easily recognizable markers. The markers were designed as small bumps that are like approximate spheres. Here, 620 markers with a diameter of less than 2 mm are located separately on both the front and back pieces of the tight dress at the abdominal part.

The implementation of each test comprises the following four consecutive steps:

1. Separate extraction of the feature points in the reference and deformed images using the Harris method.

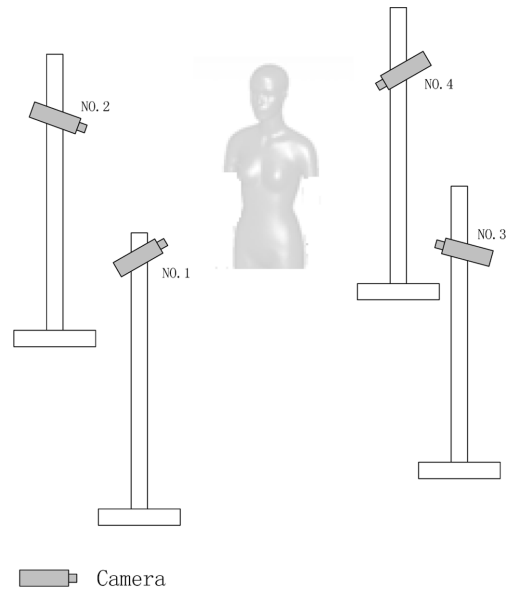


**Fig. 7.** Stereo-vision system.

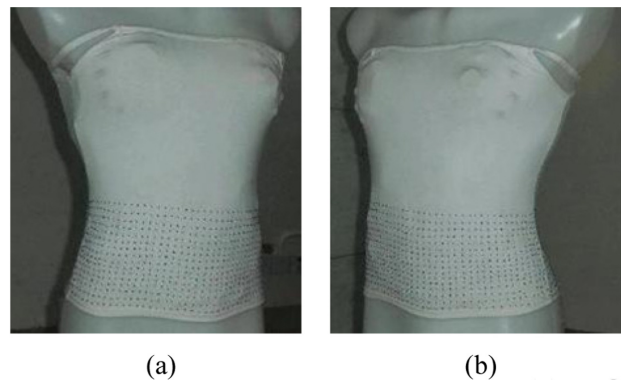


**Fig. 8.** Images from different views. (a) Frontal abdomen in left view (a) and right view (b).

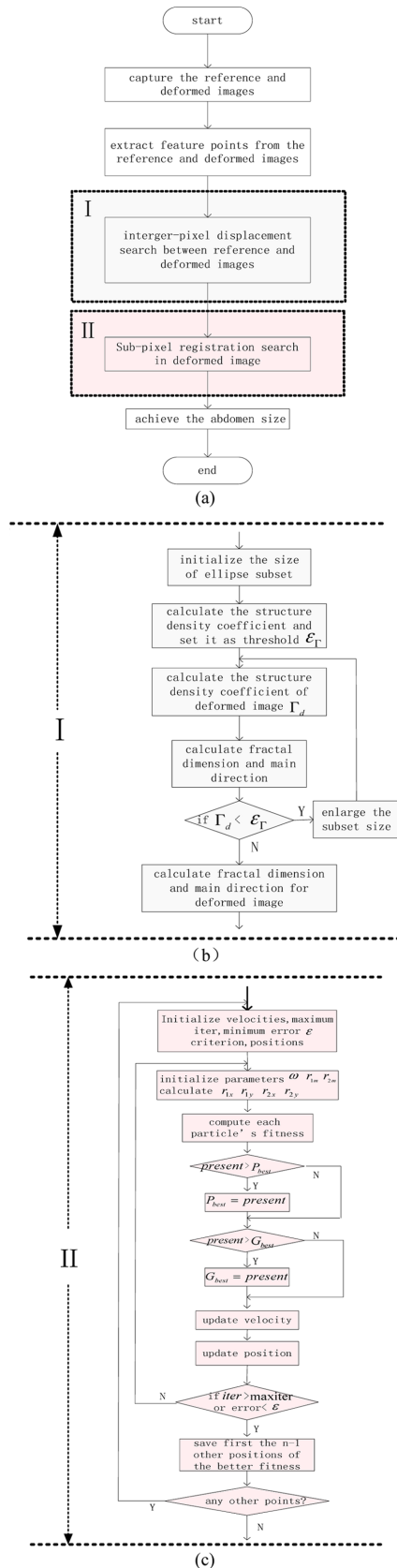


Fig. 9. Flow chart. (a) Deformation matching, (b) integral-pixel deformation, and (c) subpixel registration.

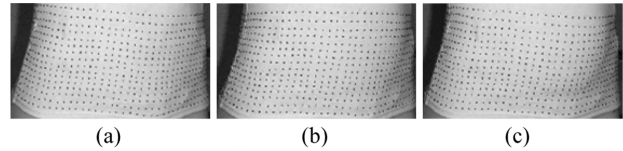


Fig. 10. Abdominal images from the left camera under different conditions. (a) Initial abdomen, (b) 10-kPa abdomen, and (c) 20-kPa abdomen.

2. Conduction of coarse tracking using the novel feature vector combined with the fractal dimension and the main direction to gain the integral-pixel positions.

3. Employment of the integral-pixel position as the initial-guess-value estimation for the subpixel fine search in the application of the MLADPSO.

4. Attainment of the various abdominal sizes that are associated with different barometric pressures by means of the recovery of a 3D abdominal model that is based on the stereo-vision system.

A flow chart is given in Fig. 9. The following subsections offer several tests regarding two typical cases in accordance with the different barometric-pressure choices. The concrete instructions are given as follows: the image shown in Fig. 10(a) shows the initial condition without any pressure in the abdominal airbag; Case 1, which is shown in Fig. 10(b), is the condition with the pressure of 10 kPa, and Case 2, which is shown in Fig. 10(c), shows the condition with the 20-kPa pressure. With the increase in the pressure, the deformation of the abdominal shape gradually occurred.

### B. Integer-Pixel Displacement Search

In this subset, a coarse displacement search is performed in comparison with the conventional method that is based on the gray-level intensity within a fixed rectangle subset and the proposed method in the previously mentioned two cases. The coordinate errors in Tables 1–3 were calculated according to all of the mismatches from the initial matching in the integer-pixel displacement.

The contrast between the performance indicators with the specific parameters that are between the two approaches is listed in Table 1. *correct\_match* is the correct matching rate that signifies the ratio of the number of absolute correct matching pairs without any errors to the total number of matched pairs. *recall\_ratio* is the entire detectability that is determined by the ratio of the correct matched points to the total number of detected feature points. *T* denotes the mapping time-consumption. *Dev\_x* and *Dev\_y* are the errors of the integer pixel from the calculated value to the real value at the x-coordinate and the y-coordinate, respectively; here, *Mean\_x* and *Std\_x* denote the average error and the variance error of the x-coordinate, respectively, and the same meanings are applicable to the *Mean\_y* and *Std\_y* of the y-coordinate. As



**Table 1.** Analysis of coordinate errors between two cases in integer-pixel

| parameters         |                   |        | traditional method | proposed method |        |
|--------------------|-------------------|--------|--------------------|-----------------|--------|
| correct_match (%)  |                   |        | 70.11              | 95.36           |        |
| recall_ratio (%)   |                   |        | 67.21              | 89.55           |        |
| reference & case 1 | T (s)             |        | 185.78             | 187.13          |        |
|                    | Dev_X (pixel)     | Mean_X | 83.64              | 15.92           |        |
|                    |                   | Std_X  | 90.19              | 11.56           |        |
|                    | Dev_Y (pixel)     | Mean_Y | 97.20              | 16.71           |        |
|                    |                   | Std_Y  | 70.07              | 12.41           |        |
|                    | correct_match (%) |        |                    | 66.05           | 94.40  |
|                    | recall_ratio (%)  |        |                    | 64.50           | 88.12  |
|                    | T (s)             |        |                    | 288.91          | 302.32 |
| reference & case 2 | Dev_X (pixel)     | Mean_X | 145.8              | 24.97           |        |
|                    |                   | Std_X  | 111.99             | 16.61           |        |
|                    | Dev_Y (pixel)     | Mean_Y | 121.64             | 27.72           |        |
|                    |                   | Std_Y  | 67.34              | 21.59           |        |

**Table 2.** Comparison of the distance error between two methods at Case 1 (pixels)

| number | real value                     |     | traditional method |     | proposed method |     | distance_t | distance_p |
|--------|--------------------------------|-----|--------------------|-----|-----------------|-----|------------|------------|
|        | X                              | Y   | X                  | Y   | X               | Y   |            |            |
| 1      | 47                             | 286 | 199                | 336 | 69              | 308 | 160.01     | 31.11      |
| 2      | 51                             | 194 | 62                 | 177 | 65              | 182 | 20.25      | 18.44      |
| 3      | 86                             | 226 | 242                | 100 | 107             | 244 | 200.53     | 27.66      |
| 4      | 137                            | 218 | 218                | 256 | 165             | 247 | 89.47      | 40.31      |
| 5      | 148                            | 181 | 466                | 280 | 161             | 166 | 333.05     | 19.85      |
| 6      | 174                            | 141 | 145                | 291 | 220             | 180 | 152.78     | 60.31      |
| 7      | 232                            | 272 | 392                | 245 | 240             | 282 | 162.26     | 12.81      |
| 8      | 246                            | 54  | 176                | 120 | 209             | 97  | 96.21      | 56.73      |
| 9      | 260                            | 161 | 355                | 204 | 286             | 142 | 104.28     | 32.20      |
| 10     | 315                            | 183 | 504                | 334 | 319             | 181 | 241.91     | 4.47       |
| 11     | 372                            | 319 | 173                | 256 | 371             | 318 | 208.73     | 1.41       |
| 12     | 384                            | 279 | 301                | 125 | 393             | 290 | 174.94     | 14.21      |
| 13     | 379                            | 204 | 527                | 268 | 396             | 228 | 161.25     | 29.41      |
| 14     | 455                            | 108 | 322                | 147 | 461             | 104 | 138.60     | 7.21       |
| 15     | 481                            | 210 | 493                | 130 | 491             | 222 | 80.89      | 15.62      |
| 16     | 489                            | 339 | 384                | 279 | 481             | 329 | 120.93     | 12.81      |
| 17     | 531                            | 254 | 494                | 108 | 549             | 287 | 150.62     | 37.59      |
| 18     | 553                            | 183 | 558                | 146 | 550             | 181 | 37.34      | 3.61       |
| 19     | 562                            | 197 | 228                | 292 | 586             | 224 | 347.25     | 36.12      |
| 20     | 573                            | 126 | 551                | 258 | 607             | 164 | 133.82     | 50.99      |
| 21     | 577                            | 312 | 523                | 310 | 574             | 312 | 54.03      | 3.00       |
| 22     | 587                            | 248 | 558                | 146 | 599             | 258 | 106.04     | 15.62      |
| 23     | 597                            | 228 | 561                | 257 | 603             | 235 | 46.23      | 9.22       |
| 24     | 605                            | 114 | 597                | 228 | 617             | 127 | 114.28     | 17.69      |
|        | minimal distance               |     |                    |     |                 |     | 20.25      | 1.41       |
|        | maximal distance               |     |                    |     |                 |     | 347.25     | 60.31      |
|        | mean distance                  |     |                    |     |                 |     | 143.15     | 23.85      |
|        | standard deviation of distance |     |                    |     |                 |     | 81.86      | 18.47      |

illustrated in Table 1, it is evident that the *correct\_match* and the *recall\_ratio* that were obtained using the proposed method are superior to those of the traditional method in both experiments, particularly under the large-deformation situation. That is, the previous two performance parameters were successfully implemented using the conventional solution that yielded sharp declines of different extents, whereas the proposed method produced

**Table 3.** Comparison of the distance error between two methods at Case 2 (pixels)

| number | real value                     |     | traditional method |     | proposed method |     | distance_t | distance_p |
|--------|--------------------------------|-----|--------------------|-----|-----------------|-----|------------|------------|
|        | X                              | Y   | X                  | Y   | X               | Y   |            |            |
| 1      | 44                             | 276 | 150                | 308 | 74              | 313 | 110.72     | 47.63      |
| 2      | 50                             | 179 | 58                 | 163 | 71              | 195 | 17.89      | 26.40      |
| 3      | 80                             | 215 | 227                | 97  | 115             | 254 | 188.50     | 52.40      |
| 4      | 126                            | 209 | 249                | 219 | 155             | 241 | 123.41     | 43.19      |
| 5      | 137                            | 172 | 319                | 313 | 112             | 189 | 230.23     | 30.23      |
| 6      | 163                            | 136 | 318                | 34  | 204             | 185 | 185.55     | 63.89      |
| 7      | 204                            | 119 | 330                | 336 | 211             | 128 | 250.93     | 11.40      |
| 8      | 220                            | 266 | 379                | 249 | 242             | 278 | 159.91     | 25.06      |
| 9      | 231                            | 52  | 277                | 181 | 269             | 94  | 136.96     | 56.64      |
| 10     | 246                            | 100 | 184                | 248 | 273             | 121 | 160.46     | 34.21      |
| 11     | 271                            | 204 | 359                | 63  | 295             | 229 | 166.21     | 34.66      |
| 12     | 291                            | 241 | 242                | 142 | 304             | 148 | 110.46     | 93.90      |
| 13     | 297                            | 208 | 271                | 56  | 311             | 298 | 154.21     | 91.08      |
| 14     | 301                            | 184 | 215                | 284 | 313             | 193 | 131.89     | 15.00      |
| 15     | 333                            | 313 | 472                | 220 | 361             | 337 | 167.24     | 36.88      |
| 16     | 348                            | 278 | 354                | 293 | 367             | 263 | 16.16      | 24.21      |
| 17     | 365                            | 210 | 261                | 182 | 394             | 241 | 107.70     | 42.45      |
| 18     | 443                            | 121 | 112                | 205 | 424             | 143 | 341.49     | 29.07      |
| 19     | 472                            | 220 | 348                | 278 | 479             | 231 | 136.89     | 13.04      |
| 20     | 486                            | 143 | 497                | 316 | 487             | 157 | 173.35     | 14.04      |
| 21     | 475                            | 339 | 209                | 232 | 460             | 322 | 286.71     | 22.67      |
| 22     | 520                            | 257 | 341                | 207 | 538             | 291 | 185.85     | 38.47      |
| 23     | 548                            | 190 | 130                | 192 | 579             | 218 | 418.00     | 41.77      |
| 24     | 556                            | 202 | 440                | 322 | 608             | 242 | 166.90     | 65.60      |
| 25     | 568                            | 131 | 553                | 258 | 581             | 145 | 127.88     | 19.10      |
| 26     | 570                            | 311 | 352                | 338 | 572             | 312 | 219.67     | 2.24       |
| 27     | 581                            | 248 | 130                | 192 | 604             | 231 | 454.46     | 28.60      |
| 28     | 590                            | 242 | 561                | 273 | 601             | 236 | 42.45      | 12.53      |
| 29     | 601                            | 115 | 569                | 45  | 583             | 141 | 76.97      | 31.63      |
|        | minimal distance               |     |                    |     |                 |     | 16.16      | 2.24       |
|        | maximal distance               |     |                    |     |                 |     | 454.46     | 93.91      |
|        | mean distance                  |     |                    |     |                 |     | 174.11     | 36.14      |
|        | standard deviation of distance |     |                    |     |                 |     | 101.63     | 22.14      |

results that maintained a greater stability and a robustness with a mere slight decrease. Moreover, the deviations of the x and y locations of the proposed method are all dramatically smaller than those of the traditional approach despite the slightly longer time-consumption that was measured within an acceptable range. Overall, it is firmly believed that the proposed method is a valuable alternative tool for the coarse search that benefits from the extraordinary ability to achieve a high accuracy and a strong stability.

To confirm the efficiency, comparisons of 24 and 29 falsely matched pairs that were selected randomly between the two methods are given here, and the results are illustrated in Tables 2 and 3, respectively. *distance\_t* and *distance\_p* denote the distance errors from the utilizations of the traditional method and the proposed method, respectively. X and Y represent the coordinate values of the points. The statistical results given at the end of each table are the minimal distance, maximal distance, mean distance, and standard deviation of distance.

As can be easily confirmed from the tabulations, the results of the two methods in either case differ by several times; this is unlike the traditional method that produces large errors that are intensified with the increase in the

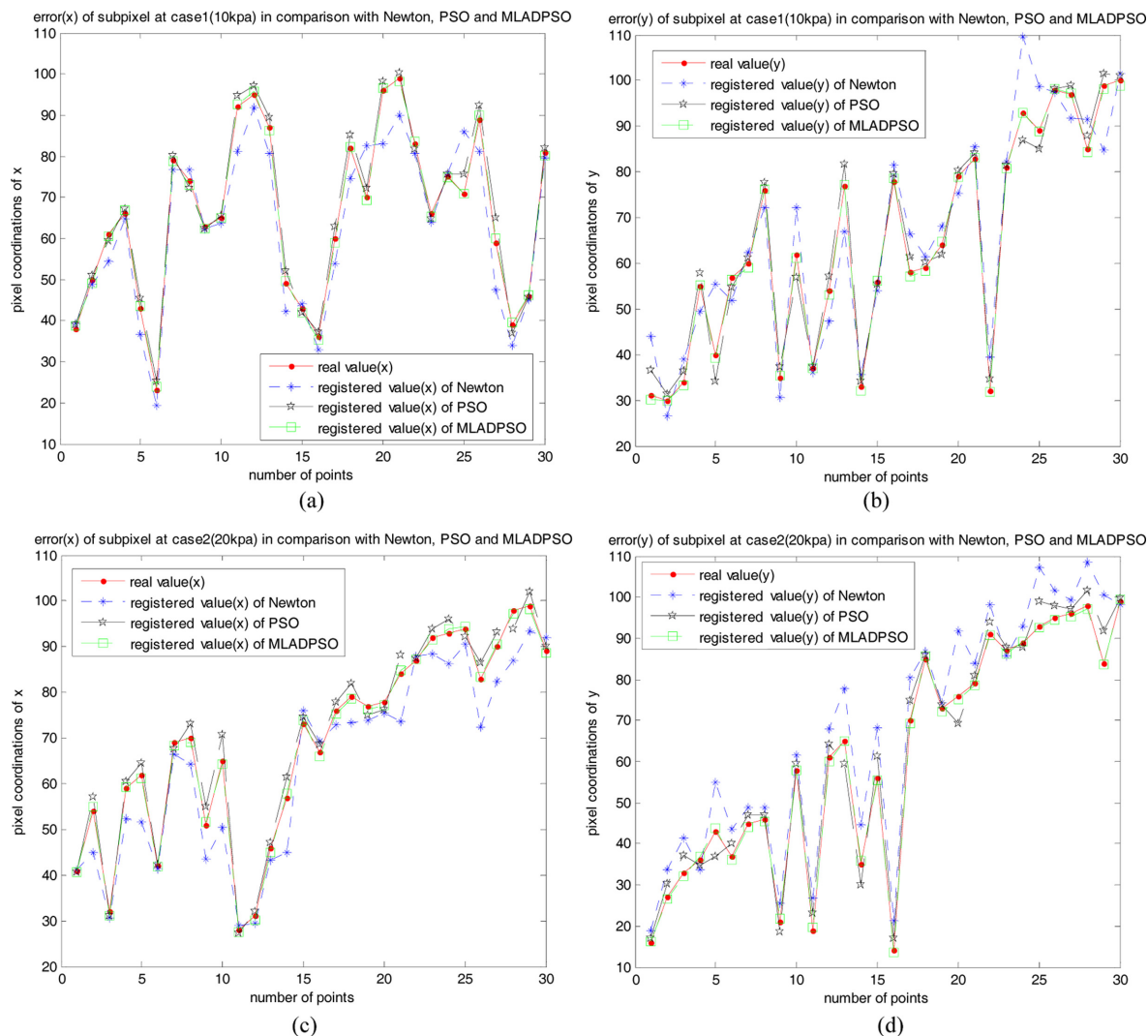


Fig. 11. Coordinate values of Case 1 and Case 2. (a, b) The x and y positions of Case 1. (c, d) The corresponding values of Case 2.

deformation. The results produced by the proposed method are basically slight deviations. This method is capable of maintaining a high stability because of the advantages of adaptability and recognition.

### C. Subpixel-Registration Algorithm

It is worth noting that, as a nonlinear optimization algorithm, the Newtonian method requires an accurate initial guess to achieve a precise and rapid convergence. In the present paper, the integer-pixel coordinate values are taken as the initial-guess estimations in the subpixel iteration. In this subsection, the focus comprises comparisons of the Newtonian method, the uniform PSO, and the proposed method, MLADPSO.

A selection of 30 feature points that were taken from the total number were enacted randomly. The specific position values of the x-coordinate and the y-coordinate that are associated with each feature point are illustrated

in Fig. 11, where Fig. 11(a) and (b) reflect the x and y positions of Case 1, and Fig. 11(c) and (d) are the corresponding values of Case 2. The results demonstrate that the MLADPSO-achieved positions are much closer to the real values than those that were obtained by the Newtonian method and PSO. With the MLADPSO, the location accuracy is up to  $10^{-6}$ , while only  $10^{-4}$  was achieved with the use of the Newtonian algorithm. The PSO accuracy is between those of the other two methods.

In addition, in consideration of a full account of the performances of the two methods, the distance errors of the subpixel as well as the time-consumption is listed below in Tables 4 and 5, respectively. The tests were conducted on two cases where the points were increased from 50 to a maximum of 497. The *mean\_dis tan ce* and *std\_dis tan ce* denote the average error and the variance of distance, respectively, while *t* is the computational time that was expended in the subpixel registration. The statistical results revealed that the MLADPSO errors are

**Table 4.** Error analysis and time-cost comparison of subpixels at Case 1 (10 kpa)

| NO  | Parameters                    | Newton  | PSO     | MLADPSO |
|-----|-------------------------------|---------|---------|---------|
| 50  | <i>mean_dis tan ce(pixel)</i> | 8.42    | 3.44    | 0.96    |
|     | <i>std_dis tan ce(pixel)</i>  | 4.44    | 1.57    | 0.20    |
|     | t(s)                          | 20.825  | 83.143  | 28.841  |
| 100 | <i>mean_dis tan ce(pixel)</i> | 8.59    | 3.69    | 0.96    |
|     | <i>std_dis tan ce(pixel)</i>  | 4.30    | 1.61    | 0.21    |
|     | t(s)                          | 41.424  | 165.696 | 46.828  |
| 200 | <i>mean_dis tan ce(pixel)</i> | 8.44    | 3.50    | 0.96    |
|     | <i>std_dis tan ce(pixel)</i>  | 4.36    | 1.53    | 0.21    |
|     | t(s)                          | 83.254  | 334.282 | 84.782  |
| 300 | <i>mean_dis tan ce(pixel)</i> | 8.28    | 3.49    | 0.96    |
|     | <i>std_dis tan ce(pixel)</i>  | 4.31    | 1.51    | 0.22    |
|     | t(s)                          | 125.112 | 512.943 | 125.038 |
| 450 | <i>mean_dis tan ce(pixel)</i> | 7.84    | 3.38    | 0.95    |
|     | <i>std_dis tan ce(pixel)</i>  | 4.31    | 1.47    | 0.21    |
|     | t(s)                          | 187.877 | 783.210 | 170.797 |
| 497 | <i>mean_dis tan ce(pixel)</i> | 7.93    | 3.37    | 0.96    |
|     | <i>std_dis tan ce(pixel)</i>  | 4.28    | 1.46    | 0.22    |
|     | t(s)                          | 219.438 | 921.915 | 190.010 |

much smaller than those of the Newtonian method and PSO in both cases.

As can be seen in the tables, at the beginning, on the condition of a small quantity, the velocity of the Newtonian method is merely faster than that of the MLADPSO; but with the increasing of the quantity, the efficiency of the MLADPSO was gradually improved. Conversely, when the number was increased to 300, the MLADPSO is faster than the Newtonian method. Overall, the PSO speeds of the three algorithms are always the slowest. This advantage is primarily attributed to the mutual-learning mechanism that contributes to the minimization of the time-consumption of the initialization for each particle, while the repetitive random initialization operations that are required for the Newtonian method waste substantial time, leading to an efficiency decline. Meanwhile, the MLADPSO improves the accuracy but reduces the running time. In general terms, the utilization of the MLADPSO is strongly recommended for the subpixel registration, especially in the case where a particularly high accuracy and efficiency are obtained.

#### D. Analysis of the Shape Size

In order to evaluate the overall accuracy of the proposed method, it was tested on a shape-flexible model. The tests were completed using the respective pressures of 10, 20, and 25 kPa and three independent modellings and measurements, and the aim is the attainment of the belly circumference in the process. In the present work, the ultimate

**Table 5.** Error analysis and time-cost comparison of subpixels at Case 2 (20 kpa)

| NO  | Parameters                    | Newton  | PSO     | MLADPSO |
|-----|-------------------------------|---------|---------|---------|
| 50  | <i>mean_dis tan ce(pixel)</i> | 10.25   | 3.89    | 0.99    |
|     | <i>std_dis tan ce(pixel)</i>  | 4.55    | 1.77    | 0.22    |
|     | t(s)                          | 21.262  | 85.039  | 29.237  |
| 100 | <i>mean_dis tan ce(pixel)</i> | 10.25   | 3.86    | 0.99    |
|     | <i>std_dis tan ce(pixel)</i>  | 4.77    | 1.73    | 0.22    |
|     | t(s)                          | 41.476  | 165.957 | 47.766  |
| 200 | <i>mean_dis tan ce(pixel)</i> | 9.14    | 3.79    | 0.98    |
|     | <i>std_dis tan ce(pixel)</i>  | 4.77    | 1.62    | 0.21    |
|     | t(s)                          | 84.364  | 342.172 | 85.766  |
| 300 | <i>mean_dis tan ce(pixel)</i> | 8.92    | 3.93    | 0.98    |
|     | <i>std_dis tan ce(pixel)</i>  | 4.39    | 1.84    | 0.21    |
|     | t(s)                          | 125.112 | 514.762 | 125.104 |
| 450 | <i>mean_dis tan ce(pixel)</i> | 8.32    | 3.85    | 0.97    |
|     | <i>std_dis tan ce(pixel)</i>  | 4.33    | 1.74    | 0.21    |
|     | t(s)                          | 189.756 | 796.975 | 173.036 |
| 497 | <i>mean_dis tan ce(pixel)</i> | 8.21    | 3.89    | 0.97    |
|     | <i>std_dis tan ce(pixel)</i>  | 4.32    | 1.83    | 0.20    |
|     | t(s)                          | 219.438 | 932.290 | 191.326 |

**Table 6.** Error inspection of the abdominal size between measured and calculated values

| Case (pressure) | Manual measured value (cm) | Proposed method value (cm) | Error (cm) | R_Error |
|-----------------|----------------------------|----------------------------|------------|---------|
| 10kpa           | 77.31                      | 77.76                      | 0.45       | 0.58%   |
| 20kpa           | 80.64                      | 81.15                      | 0.51       | 0.63%   |
| 25kpa           | 82.78                      | 83.31                      | 0.53       | 0.64%   |

abdominal size was obtained using a 3D-reconstruction technique that is based on the stereo-vision system after the completion of the coarse-fine search. The manual measurement is a traditional contact method. Comparisons of the parameters of the previous two schemes (manual measurement and the proposed method) were made. As shown in Table 6, the Error and the R\_Error are the error and the relative error between the manual and proposed methods, respectively, in the three pressure-value cases. The results listed in Table 6 revealed that even with the existence of differences from the comparison with the measured values, the errors are merely minor and completely conform to the acceptable criteria in consideration of apparel design and engineering.

## V. CONCLUSIONS

In this paper, an innovative 3D DIC formulation with a coarse-fine two-step method is proposed. Tests of the

abdominal 3D deformation measurements were carried out on a shape-flexible mannequin to validate the proposed method. The results of the integer-pixel examination revealed that the fractal dimension and the main direction are more feasible and reliable compared with those of the traditional method. The results derived from the subpixel-registration resolution demonstrated that the modified MLADPSO is more accurate with a higher computational efficiency, and this is in contrast to the Newtonian algorithm and PSO. In particular, the boosting of the iterative computations of the subpixels in the proposed method are gradual as the number of feature points are increased, and this occurs without any loss of the measurement precision.

## ACKNOWLEDGMENTS

This work was supported in part by the Key Project of the National Nature Science Foundation of China (No. 61134009, 61462046, and 61640412), Program for Changjiang Scholars from the Ministry of Education, Innovation Program of Shanghai Municipal Education Commission (No. 14ZZ067), the Natural Science Foundation of Jiangxi Province (No. 20161BAB202049 and 20161BAB204172), Humanities and Social Science project of Jiangxi College (No. YS1546), the Bidding Project of the Key Laboratory of Watershed Ecology and Geographical Environment Monitoring, NASG (No. WE2015013, WE2016003, WE2016013, and WE2016015), Science and Technology Research Projects of Jiangxi Province Education Department (No. GJJ160741), and Jinggangshan University Doctoral Scientific Research Foundation (No. JZB15016 and JZB15009).

## REFERENCES

1. H. Liu, K. R. Hao, and Y. S. Ding, "New anti-blur and illumination-robust combined invariant for stereo vision in human belly reconstruction," *The Imaging Science Journal*, vol. 62, no. 5, pp. 251-264, 2014.
2. H. Liu, Y. Xiao, W. D. Tang, and Y. H. Zhou, "Illumination-robust and anti-blur feature descriptors for image matching in abdomen reconstruction," *International Journal of Automation and Computing*, vol. 11, no. 5, pp. 469-479, 2014.
3. J. Park, S. Yoon, T. H. Kwon, and K. Park, "Assessment of speckle-pattern quality in digital image correlation based on gray intensity and speckle morphology," *Optics and Lasers in Engineering*, vol. 91, no. 1, pp. 62-72, 2016.
4. G. F. Bomarito, J. D. Hochhalter, T. J. Ruggles, and A. H. Cannon, "Increasing accuracy and precision of digital image correlation through pattern optimization," *Optics and Lasers in Engineering*, vol. 91, pp. 73-85, 2017.
5. W. H. Peter and W. F. Ranson, "Digital imaging techniques in experimental stress analysis," *Optical Engineering*, vol. 21, no. 3, pp. 427-431, 1982.
6. M. C. Weng, S. H. Tung, and M. H. Shih, "Microscopic characteristics of problematic tertiary sandstone as revealed by grain-wide local deformation," *International Journal of Rock Mechanics and Mining Science*, vol. 46, no. 7, pp. 1243-1251, 2009.
7. Z. G. Tang, J. Liang, Z. Z. Xiao, and C. Guo, "Large deformation measurement scheme for 3D digital image correlation method," *Optics and Lasers in Engineering*, vol. 50, no. 2, pp. 122-130, 2012.
8. B. Pan, D. F. Wu, H. M. Xie, and Z. X. Hu, "Spatial-gradient-based digital volume correlation technique for internal deformation measurement," *Acta Optica Sinica*, vol. 31, no. 6, article ID. 0612005, 2011.
9. B. Pan and B. Wang, "Digital image correlation with enhanced accuracy and efficiency: a comparison of two subpixel registration algorithms," *Experimental Mechanics*, vol. 56, no. 8, pp. 1395-1409, 2016.
10. M. Kimura, M. Mochimaru, and T. Kanade, "3D measurement of feature cross-sections of foot while walking," *Machine Vision and Applications*, vol. 22, no. 2, pp. 377-388, 2011.
11. M. Bornert, F. Bremond, P. Doumalin, J. C. Dupre, M. Fazzini, M. Grediac, et al., "Assessment of digital image correlation measurement errors: methodology and results," *Experimental Mechanics*, vol. 49, no. 3, pp. 353-370, 2009.
12. H. W. Schreier and M. A. Sutton, "Systematic errors in digital image correlation due to undermatched subset shape functions," *Experimental Mechanics*, vol. 42, no. 3, pp. 303-310, 2002.
13. B. Pan, H. M. Xie, Z. Y. Wang, K. M. Qian, and Z. Wang, "Study on subset size selection in digital image correlation for speckle patterns," *Optics Express*, vol. 16, no. 10, pp. 7037-7048, 2008.
14. B. Pan, H. M. Xie, B. Q. Xu, and F. L. Dai, "Performance of sub-pixel registration algorithms in digital image correlation," *Measurement Science and Technology*, vol. 17, no. 6, pp. 1615-1621, 2006.
15. B. Pan, A. Asundi, H. M. Xie, and J. X. Gao, "Digital image correlation using iterative least squares and pointwise least squares for displacement field and strain field measurements," *Optics and Lasers in Engineering*, vol. 47, no. 7-8, pp. 865-874, 2009.
16. B. Pan, K. M. Qian, H. M. Xie, and A. Asundi, "Two-dimensional digital image correlation for in-plane displacement and strain measurement: a review," *Measurement Science and Technology*, vol. 20, no. 6, article ID. 062001, 2009.
17. Q. Li, G. Zhou, and T. Xiao, "Research on high accuracy registration of dual energy CT images in synchrotron radiation," *Acta Optica Sinica*, vol. 36, no. 4, pp. 116-123, 2016.
18. J. Q. Zhao, P. Zeng, L. P. Lei, and Y. Ma, "Initial guess by improved population-based intelligent algorithm for large inter-frame deformation measurement using digital image correlation," *Optics and Lasers in Engineering*, vol. 50, no. 3, pp. 473-490, 2012.
19. W. Gao, C. Shao, and Q. Gao, "An optimization algorithm with novel flexible grid: applications to parameter decision in LS-SVM," *Journal of Computing Science and Engineering*, vol. 9, no. 2, pp. 39-50, 2015.
20. Z. F. Zhang, Y. L. Kang, H. W. Wang, Q. H. Qin, Y. Qin, and X. Q. Li, "A novel coarse-fine search scheme for digital image correlation method," *Measurement*, vol. 39, no. 8,

- pp. 710-718, 2006.
21. A. R. Backes and O. M. Bruno, "Texture analysis using volume-radius fractal dimension," *Applied Mathematics and Computation*, vol. 219, no. 11, pp. 5870-5875, 2013.
  22. Z. Shen, X. Chen, X. Tang, and H. Zhang, "Road damage feature extraction in image based on fractal dimension," *Applied Mechanics and Materials*, vol. 256-259, no. 1, pp. 2971-2975, 2013.
  23. W. K. Chen, J. C. Lee, W. Y. Han, C. K. Shih, and K. C. Chang, "Iris recognition based on bidimensional empirical mode decomposition and fractal dimension," *Information Sciences*, vol. 221, pp. 439-451, 2013.
  24. J. B. Florindo and O. M. Bruno, "Local fractal dimension and binary pattern in texture recognition," *Pattern Recognition Letters*, vol. 78, no. 15, pp. 22-27, 2016.
  25. X. Wang, N. D. Georganas, and E. M. Petriu, "Fabric texture analysis using computer vision techniques," *IEEE Transactions on Instrumentation and Measurement*, vol. 60, no. 1, pp. 44-56, 2011.
  26. A. D. C. Kamila, A. Juliana, A. P. Thais, and R. D. O. H. Luis, "3-D reconstruction by extended depth-of-field in failure analysis. Case study II: Fractal analysis of interlaminar fracture in carbon/epoxy composites," *Engineering Failure Analysis*, vol. 25, no. 1, pp. 271-279, 2012.
  27. B. Pan and K. A. Li, "A fast digital image correlation method for deformation measurement," *Optics and Lasers in Engineering*, vol. 49, no. 7, pp. 841-847, 2011.
  28. Y. F. Hu, "Research on a three-dimensional reconstruction method based on the feature matching algorithm of a scale-invariant feature transform," *Mathematical and Computer Modelling*, vol. 54, no. 3-4, pp. 919-923, 2011.
  29. R. Cheng, Y. Zhao, Z. Li, W. Jiang, X. A. Wang, and Y. Xu, "Panorama parking assistant system with improved particle swarm optimization method," *Journal of Electronic Imaging*, vol. 22, no. 4, pp. 451-459, 2013.
  30. L. C. Geng, S. Z. Su, and D. B. Cao, "Perspective-invariant image matching framework with binary feature descriptor and APSO," *International Journal of Pattern Recognition and Artificial Intelligence*, vol. 28, no. 8, article ID. 1455011, 2014.



### Liu Huan

Liu Huan graduated from Nanjing Institute of Technology, China in 2004. She received the M.S. degree from Jiangxi Normal University, China in 2008 and the Ph.D. degree from Donghua University, China in 2014. She is currently a lecturer at Jinggangshan University. Her research interests include machine vision, image processing and intelligent algorithm. E-mail: liuhuan816618@163.com



### Kuangrong Hao

Kuangrong Hao is currently a Professor at the College of Information Sciences and Technology, Donghua University, Shanghai, China. She obtained her B.S. degree in Mechanical Engineering from Hebei University of Technology, Tianjin, China in 1984, her M.S. degree from Ecole Normale Supérieure de Cachan, Paris, France in 1991, and her Ph.D. degree in Mathematics and Computer Science from Ecole Nationale des Ponts et Chaussées, Paris, France in 1995. She has published more than 100 technical papers, and two research monographs. Her scientific interests include machine vision and image processing, robot control, intelligent control, digitized textile technology.



### Yongsheng Ding

Yongsheng Ding (M'00-SM'05) is currently a Professor at College of Information Sciences and Technology, Donghua University, Shanghai, China. He obtained the B.S., M.S., and Ph.D. degrees in Electrical Engineering from Donghua University, Shanghai, China in 1989, 1994, and 1998, respectively. From 1996 to 1998, he was a Visiting Scientist at Biomedical Engineering Center, The University of Texas Medical Branch, TX, USA. From February 2005 to April 2005, he was a Visiting Professor at Department of Electrical and Computer Engineering, Wayne State University, MI, USA. From September 2007 to February 2008, he was a Visiting Professor at Harvard Medical School, Harvard University, MA, USA. He serves as Senior Member of Institute of Electrical and Electronics Engineers (IEEE). He has published more than 300 technical papers, and five research monograph/advanced textbooks. His scientific interests include computational intelligence, network intelligence, nature-inspired technologies, intelligent robots, Internet of things, bio-informatics, and digitized textile technology.